



2D carbide nanomeshes and their assembling into 3D microflowers for efficient water splitting

Zongkui Kou^{a,*}, Lei Zhang^{a,1}, Yuanyuan Ma^{a,1}, Ximeng Liu^a, Wenjie Zang^a, Jian Zhang^b, Shaozhan Huang^c, Yonghua Du^d, Anthony K. Cheetham^a, John Wang^{a,*}

^a Department of Materials Science and Engineering, National University of Singapore, 117574, Singapore

^b School of Materials Science and Engineering, Nanyang Technological University, 639798, Singapore

^c Pillar of Engineering Product Development, Singapore University of Technology and Design, 487372, Singapore

^d Institute of Chemical and Engineering Sciences, A*STAR, 1 Pesek Road, Jurong Island, 627833, Singapore

ARTICLE INFO

Keywords:

Surface engineering

2D carbide

Nanomesh

3D assembly

Water splitting

ABSTRACT

Herein, we have developed a facile process of synthesizing N and O surface-terminated 2D molybdenum carbide nanomeshes (Mo_2CT_x NMs) and assembling them into 3D microflowers (Mo_2CT_x MFs) by one-step pyrolysis of Mo/Zn bimetallic imidazolate frameworks. When used as an oxygen evolution reaction (OER) catalyst, the Mo_2CT_x NMs thus derived exhibit outstanding catalytic activity with an overpotential of 180 mV at the current density of 10 mA cm^{-2} . This enables Mo_2CT_x NMs to become one of the best OER electrocatalysts ever reported, with the desired stability in alkaline environment which is a major challenge for most of the non-oxide/hydroxide based electrocatalysts. Additionally, the Mo_2CT_x MFs can catalyze the hydrogen evolution reaction (HER) and act as bifunctional electrocatalysts for overall water splitting which can attain a current density of 10 mA cm^{-2} at 1.7 V. Mo LIII-edge X-ray near-edge absorption studies combined with theoretical calculations imply that surface-terminated oxygen is crucial in activating the outstanding OER performance, whereas the top Mo atomic sites on the surface contribute to excellent HER performance.

1. Introduction

Water splitting has been regarded as one of the most promising technology towards chemical energy production [1,2]. As two key and complex half reactions, the oxygen and hydrogen evolution reactions (OER and HER) occur at the anode and cathode, respectively [3–5]. Effective bifunctional catalyst with promising activity is imperative to reduce the large overpotentials. Traditionally, noble Ir-based and Pt-based catalysts are catalyzing the respective OER and HER processes. However, the high cost and low reserves of these noble metals apparently limit their practical use in large scale [6,7]. In recent decades, a large group of active non-noble catalysts have been reported, examples of which being perovskite oxides [8] and transition metal oxides [9,10] /hydroxides [11] for the alkaline OER, and transition metal sulfides [12], phosphides [13], nitrides [14], carbides [15,16], selenides [17] and borides [18] for the acidic HER. For practically useful applications in large scales, OER and HER should be preferably catalyzed in the same solution, especially a base environment. Nevertheless, this target retains a formidable task for the majority of those well-stocked

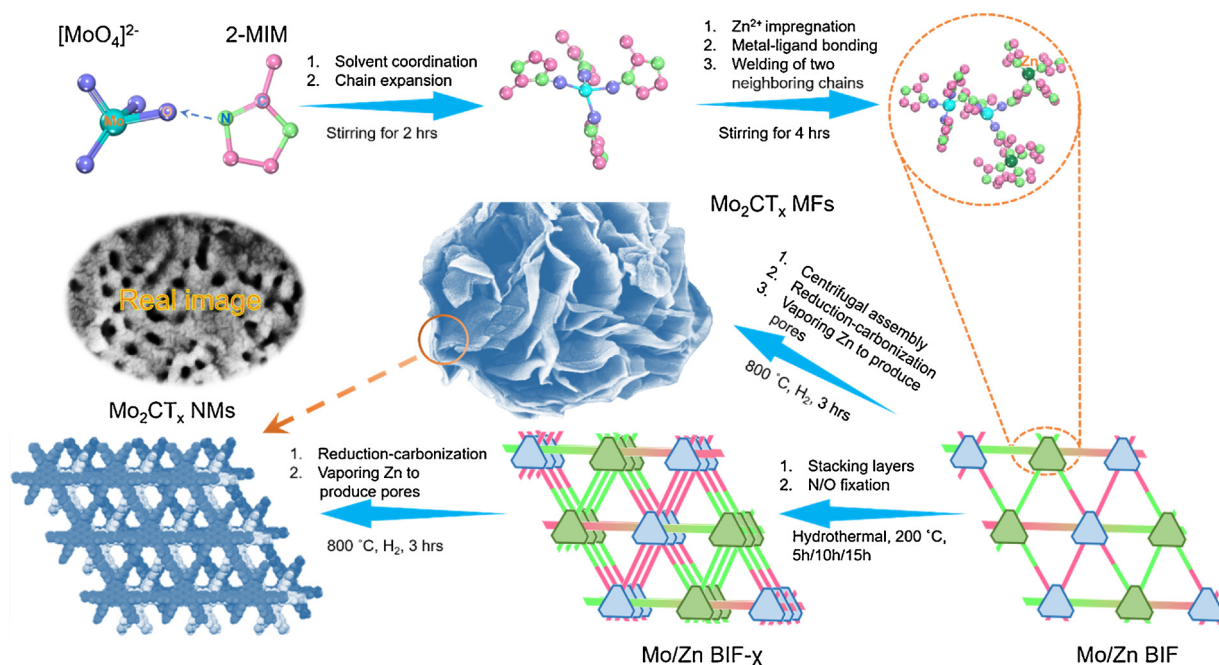
electrocatalysts (e.g. Mo_2C), since a remarkably active catalyst in acid can be rather inactive in base. Although the modest progress has been achieved to date, the development of new bifunctional electrocatalysts with outstanding activity and robustness toward overall water splitting in base remains an important challenge.

Transition metal carbides (TMCs) have recently gained popular attention on account of their noteworthy catalytic activity, robust structural stability, and abundant resource [19]. As molybdenum presents a Pt-like d-band electronic structure when combined with carbon atoms, molybdenum carbide (Mo_2C) has been investigated as a highly active HER electrocatalyst in pH-universal electrolytes [20,21]. Recently, 2D TMCs have been studied theoretically and first explored as HER catalyst in an acidic electrolyte [22]. Moreover, the combination of carbon nitride and 2D titanium carbide nanosheets has been shown to be an effective OER catalyst due to the presence of abundant and active Ti-N_x moieties [23]. However, due to the limitations of the available synthesis approaches, the resultant 2D carbides are dense rather than porous, and inclined to stack together as well as with inactive surfaces [24]. This leads to a poor balance of mass transfer and density of active sites as

* Corresponding authors.

E-mail addresses: msekz@nus.edu.sg (Z. Kou), msewangj@nus.edu.sg (J. Wang).

¹ These authors contributed equally to this work.



Scheme 1. Schematic illustration of the synthetic process for 2D molybdenum carbide nanomeshes (Mo₂CT_x NMs) and assembled 3D microflowers (Mo₂CT_x MFs). They are derived from a novel Mo/Zn bimetallic imidazole framework (Mo/Zn BIF) which is obtained by a two-step reaction at room temperature. χ represents different hydrothermal time.

well as catalytic capability for water splitting. To address this bottleneck problem, one approach is to develop abundant mesopores on the surfaces of 2D materials and then integrate them into open 3D scaffolds [25–28]. They can also promote ionic transport and accelerate electron transfer. Additionally, further surface engineering at atomic-scale [29] of the 3D structures assembled from porous 2D nanomaterials can give rise to the desired multiscale modulation to synergistically boost the OER/HER electrochemical process. However, such highly desired all-round structural control and surface engineering within carbides to enhance the electrocatalytic performance has not been reported to date.

As a proof of concept, we develop a pyrolysis route starting from a Mo/Zn bimetallic imidazolate frameworks precursor to realize multiscale structural controls and surface engineering of 2D Mo₂C towards highly efficient overall water splitting. The system thus developed has several important features: (i) at the macro-scale, porous 2D Mo₂C nanomeshes (Mo₂CT_x NMs, T_x represents two surface terminations, namely O and N) and corresponding 3D microflowers (Mo₂CT_x MFs) facilitate the transport of reactive OH⁻ and H₃O⁺ as well as the O₂ and H₂ that are produced, while increasing the accessibility to the Mo₂C surface; (ii) at the nanoscale, interlocking Mo₂C domains around the pores enhance the electrochemical robustness and the amount of active sites; and (iii) at the atomic-scale, surface engineering with O attached into the Mo₂CT_x NMs and MFs improves the intrinsic OER activity and stability, while the abundant Mo atomic sites on the surfaces of the Mo₂C domains promote the HER process. Taking overall advantage of the structural controls and surface engineering of Mo₂C, such Mo₂CT_x NMs electrocatalysts with highly active surfaces exhibit excellent durability and an ultralow overpotential of only 180 mV to drive a current density of 10 mA cm⁻², outperforming most of the other reported OER electrocatalysts in basic electrolytes. Additionally, the Mo₂CT_x MFs can efficiently catalyze the HER in base which only require an overpotential of 140 mV to obtain a current density of 10 mA cm⁻². Further, we achieve a current density of 10 mA cm⁻² at 1.7 V by using the Mo₂CT_x MFs as both the cathode and the anode for overall water splitting. Significantly, we have disclosed the essence of the excellent catalytic activity towards OER/HER by conducting Mo LIII-edge X-ray near edge absorption analysis combined with theoretical calculations. The

strategies presented in this work can broaden the new way for the fine design of 2D carbide electrocatalysts through multiscale structural controls and surface engineering that can boost the electrocatalytic performance and long-term stability. The concept can be further extended to other advanced nanomaterials of electrocatalysts.

2. Materials and methods

2.1. Materials

Zinc nitrate hexahydrate (Zn(NO₃)₂·6H₂O; ≥99.0%), 2-methylimidazole (2-mIm; 99.0%), ammonium molybdate ((NH₄)₆Mo₇O₂₄·4H₂O, 99.0%) were purchased from Sigma-Aldrich Co., Ltd. and directly used without any purification. The DI water with the resistivity of 18.25 MΩ cm⁻¹ was purified with a water ultrapure cation system.

2.2. Synthesis of Mo/Zn bimetal imidazole frameworks (Mo/Zn BIF)

(NH₄)₆Mo₇O₂₄·4H₂O (1.96 g), 2-mIm (1.3 g) and DI water (40 ml) were mixed into a 100 mL beaker and then under stirring for 2 h. Next, the Zn(NO₃)₂·6H₂O (0.59 g) was added to the above solution and 40 ml DI water was subsequently added. The solution was then stirred for 4 h. Finally, the product was collected after repeated centrifugation (8000 rpm, 10 min) and washed 3 times with DI water and ethyl alcohol, respectively, and then dried in an oven at 70 °C overnight.

2.3. Synthesis of Mo/Zn BIF-χ

The preparation process was similar to that of Mo/Zn BIF, except that a hydrothermal reaction was conducted before centrifugation. The hydrothermal temperature was controlled at 200 °C. χ represents the hydrothermal time, which was 5, 10 or 15 h.

2.4. Synthesis of 2D molybdenum carbide nanomeshes (Mo₂CT_x NMs) and assembled 3D microflowers (Mo₂CT_x MFs)

The Mo₂CT_x NMs and MFs were respectively obtained by heating

the corresponding Mo/Zn BIF- χ and Mo/Zn BIF samples at 800 °C and holding for 3 h in the hybrid atmosphere of 10% H₂ in Ar. Note that MoO₂ nanomeshes (MoO₂ NMs) could form under a mixed Ar/O₂ atmosphere.

3. Results

3.1. Synthesis and characterization of molybdenum carbide nanomeshes and microflowers

The 2D molybdenum carbide nanomeshes and microflowers (Mo₂CT_x NMs and MFs) were prepared by the synthesis procedure illustrated in Scheme 1. First, (NH₄)₆Mo₇O₂₄ and 2-methylimidazole (2-mIm) in the appropriate proportions were slowly added into DI water and stirred for 2.0 h. This gave rise to a homogeneous cross-link reaction and chain expansion, where MoO₄^{2−} is bonded to 2-mIm molecules (see Fourier transform infrared spectroscopy (FTIR) in Figure S1), in accordance with previous findings [30]. Zn(NO₃)₂·6H₂O was then introduced into the above solution and furtherly stirred for 4.0 h; the Zn ions coordinate with 2-mIm [31] (Figure S1) and link neighboring chains, leading to the formation of a 3D assembly with a sheet-like Mo/Zn bimetallic imidazolate framework (Mo/Zn BIF). This can be confirmed by powder X-ray diffraction (PXRD, Figure S2) and field-emission scanning electron microscopy (FESEM) analyses (Figure S3). The resulting Mo/Zn BIF assembly was then subjected to reduction-carbonization at 800 °C under a H₂/Ar hybrid atmosphere, causing Zn atoms to distill out of the structure to produce the desired pores. During this process, C atoms are activated and diffuse into the intermediate MoO_x lattice [16], reducing it to form Mo₂CT_x MFs.

On account of the high volatility of N/O-containing moieties from the Mo/Zn BIF [32] during the final high-temperature pyrolysis, a hydrothermal reaction was conducted to pre-stabilize N/O species in the Mo/Zn BIF. As a result, although the hydrothermal reaction leads to slight stacking of the sheet-like Mo/Zn BIF (Figure S4), it efficiently increases the N/O content of the Mo/Zn BIF while not destroying the coordination bonds (Figures S1, S5 and S6). It is of interest to note that the hydrothermal reaction time is crucial in controlling the integrity of Mo/Zn BIF sheets and the N/O concentrations on the surfaces of the final product. With increasing hydrothermal reaction time, the resultant samples (denoted as Mo/Zn BIF- χ , χ representing hydrothermal reaction time of 5, 10 and 15 h) appear almost the same as each other whereas the integrity of the Mo/Zn BIF sheets (Figure S7) and the surface terminating N/O level of the final products increase with the time (Table S1). The same high temperature reduction-carbonization process was used to transform the various Mo/Zn BIF- χ samples into corresponding Mo₂CT_x NMs- χ , as confirmed by FESEM techniques (Figure S8). Moreover, the key effect of reductive H₂ on the formation of the Mo₂C phase has been verified by substituting with a mixed Ar/O₂ gas (Figure S9).

The morphology of the Mo₂CT_x NMs and MFs was first characterized by FESEM (Fig. 1a–d). The Mo₂CT_x NMs fabricated in the present study are composed of irregular large mesopores that are randomly distributed on the surfaces of Mo₂CT_x nanoflakes (Fig. 1a and Figure S10a), while the resulting Mo₂CT_x MFs consist of assembled Mo₂CT_x thin sheets in random directions (Fig. 1b–c). The energy-dispersive spectroscopy (EDS) elemental mapping images of both Mo₂CT_x NMs (Figure S10b–f) and MFs (Fig. 1d–i) show that the C, N, O and Mo elements are distributed respectively across the whole nanomeshes and microflowers, indicating the successful evolution from the Mo/Zn BIF precursors to N and O surface-terminated Mo₂CT_x NMs and the assembled MFs. Importantly, EDX spectrum analysis (Fig. 1e and Figure S10b) suggests that the hydrothermal reaction could pre-stabilize O species in the Mo/Zn BIF and thus increase the O content of the Mo₂CT_x NMs (10.37 at%) compared with the Mo₂CT_x MFs (7.45 at%). Studies using high resolution FESEM (Fig. 1j) reveal that assembled nanosheets contain plenty of smaller mesopores than the Mo₂CT_x NMs which could

well be produced from the vaporization of Zn during reduction-carbonization of Mo/Zn BIF [31].

The microstructure of the Mo₂CT_x NMs and MFs is further confirmed by transmission electron microscopy (TEM), high resolution TEM (HRTEM), and atomic level high-angle annular dark field-scanning TEM (HAADF-STEM). As shown in Fig. 1k and Figure S10g, the sheet-like mesoporous structure could be clearly visible. The HRTEM image presents that the Mo₂C domains exhibit the interlayer spacing of 2.3 Å which is assigned to the (111) plane of Mo₂C (Fig. 1l and m, Figure S10h and i). Correspondingly, the selected-area electron diffraction (SAED) image discloses the hexagon diffraction spots of the (111) facets of Mo₂C, confirming its excellent monocrystalline nature (Fig. 1n and Figure S10j). The atomic level HAADF-STEM image (Fig. 1o) reveals the existence of micropores among interconnected Mo₂C domains (the red arrows), which would favor fast ion transport in the electrochemical reactions [33]. Moreover, it can be seen that all the Mo atoms are closely packed into a hexagonal structure (Fig. 1p), indicating a Mo metal-faceted Mo₂C which has been demonstrated to be more active towards electrocatalytic reaction than the C-facets [34] in the carbides.

We also examined the chemical nature of the final products using PXRD and Raman spectroscopy. From PXRD patterns (Fig. 2a and Figure S11), except for the broad signal at 13.7° from a Mo₂C MXene phase which could be produced by partially ordered stacking of Mo₂C nanosheets [35], all the diffraction peaks are assignable to Mo₂C with no sign of the formation of other phases. Only Mo₂C peaks at 282, 662, 819, 992 cm^{−1} can be observed in the Raman spectrum (Fig. 3b and Figure S12), indicating a pure phase Mo₂C in the final products. To gain insight into the various chemical termination species on the surfaces of the Mo₂CT_x MFs and NMs, X-ray photoelectron spectroscopy (XPS) was performed (Fig. 2c–d and Figures S13–14). The fitting of the Mo 3d signal shows the four states (+2, +3, +5 and +6) for Mo on the surface (Fig. 2d). The Mo⁶⁺ and Mo⁵⁺ most probably arise from surface terminations species (e.g. O and OH) in the final product [36]. Moreover, their percentages increase with hydrothermal time (Table S1) indicating that hydrothermal reactions are crucial in the immobilization of surface oxygen terminations. The peak fitting of the C 1s region (Figure S15) presents that is consisting of C=O, C–N and C–C/C=C species [37]. The absence of Mo–C species [38] implies that Mo²⁺ and Mo³⁺ could result from N coordination. Furtherly, the N 1s–Mo 3p spectrum (Fig. 2e) also reveals the strongest peak of N–C (1s at 398.7 eV), and another peak of Mo–N (3p3/2 at 394.5 eV) [39]. To further clarify the oxygen terminations, O 1s core level XPS spectra of Mo₂CT_x NM and MF is presented in Fig. 2f. The main peak at 531 eV is assigned to Mo₂CO_x (O terminated) [38], providing a useful clue on oxygen terminations. All the above results confirm the formation of N and O surface-terminated Mo₂CT_x NMs and assembled 3D Mo₂CT_x MFs with dominant Mo metal facets.

3.2. Electrocatalytic OER, HER and overall water splitting performance of Mo₂CT_x NMs and MFs

To test the catalytic activities toward OER, all the products were added dropwise onto common 1*2 Ni foams (Figure S16). The as-prepared catalysts were tested in 1 M KOH solution. All the potentials are normalized to the reversible hydrogen electrode (RHE) (see Methods in the Supporting Information). Mo₂CT_x MFs indicate a low onset potential around 1.39 V (Fig. 3a) and a Tafel slope of 66 mV decade^{−1} (Fig. 3b). The OER performance of Mo₂CT_x NMs with an onset potential of 1.38 V and ultralow Tafel slope of 36 mV decade^{−1} is significantly better than those of the assembled MFs. Note that the increased levels of surface terminated oxygen species could be responsible for the enhanced OER performance. Significantly, the OER activity can be increased to achieve the anodic current density of 10 mA cm^{−2} at an ultralow overpotential of 180 mV. To evaluate the intrinsic activity of Mo₂CT_x NMs, the O₂ turnover frequency (TOF) were calculated by normalizing the rate of O₂ generation to total number of

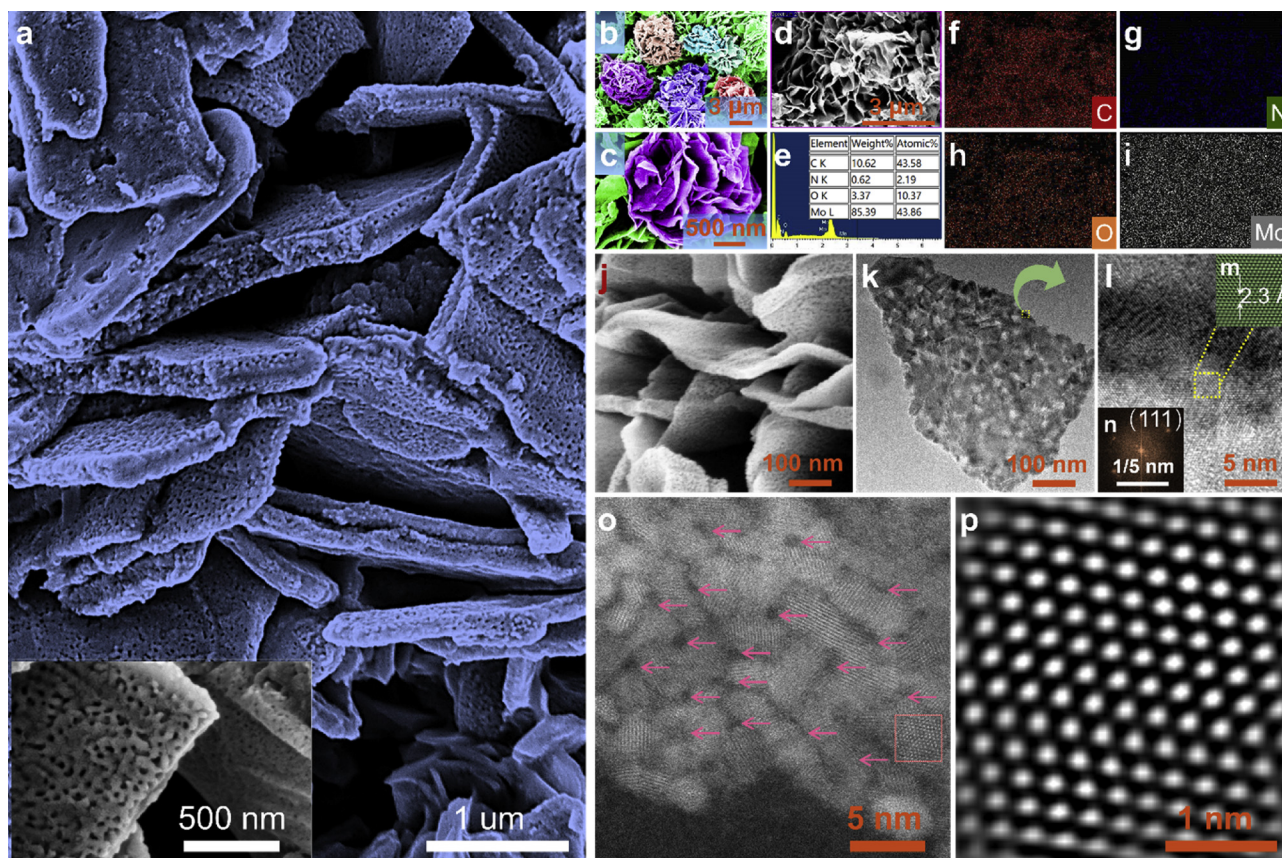


Fig. 1. Morphology and structural characterization of 2D Mo_2CT_x NMs and assembled 3D Mo_2CT_x MFs. (a) FESEM images of the Mo_2CT_x NMs. Inset: A magnified FESEM image presents a single NM. (b and c) FESEM images (b) of the Mo_2CT_x MFs and a magnified FESEM image displays a single MF. (d–i) Magnified FESEM image (d) operated at 15 kV of the Mo_2CT_x MFs which was used to collect EDX spectrum (e) and elemental mapping of carbon (f), nitrogen (g), oxygen (h) and molybdenum (i). The table inset in e summarizes the weight ratio and atomic ratio of elements inside the Mo_2CT_x MFs. (j) High resolution FESEM images of the Mo_2CT_x MFs where thin NMs are assembling into MFs. (k–n) TEM (k), high resolution TEM (l), magnified counterpart (m) and SAED images (n) of the Mo_2CT_x MFs. (o and p) HAADF-STEM (o) and atomic level resolution (p) images of the Mo_2CT_x MFs.

electrochemically active sites (See details in Supplementary Information). To eliminate the influence of other possible chemical reactions and quantify the amount of produced O_2 and Faradaic efficiency (F. E.), a constant-potential measurement was conducted at the overpotential of 200 mV in a three-electrode configuration with the counter and working electrodes separated by a piece of nafion film. As shown in Figure S17, the amount of O_2 quantified by the drainage method is well matched with the theoretically calculated amount, by assuming a 100% Faradaic efficiency for the O_2 evolution. Importantly, the Mo_2CT_x NMs catalyst exhibits the remarkably higher TOF (0.0315 s^{-1}) than that of Mo_2CT_x MFs (0.0101 s^{-1}) at a low overpotential of 200 mV. In addition, the HER activity of Mo_2CT_x NMs was also measured in 1 M KOH. The results show a small onset potential of 38 mV, an overpotential of $\sim 154 \text{ mV}$ (η_{10} , Fig. 3c) at the current density of 10 mA cm^{-2} and a Tafel slope of $100 \text{ mV decade}^{-1}$ (Fig. 3d). Mo_2CT_x MFs present a better HER performance than that of the Mo_2CT_x NMs, gaining a low η_{10} of 140 mV and Tafel slope of $90 \text{ mV decade}^{-1}$.

TMCs-based HER catalysts in alkaline solutions have been extensively investigated [15,20,21,40,41], but their OER and bifunctional activities are rarely reported [42], which limits their practical application. The overall water splitting behavior of the Mo_2CT_x MFs reveals a remarkably lower onset voltage, and η_{10} than those of the Mo_2CT_x NMs (Fig. 3e). Furthermore, the mass of O_2 and H_2 bubbles can be obviously seen on the Mo_2CT_x MFs bifunctional electrodes, indicating their great capability for overall water splitting (see Movie S1 which shows how one 1.8 V battery drives overall water splitting with Mo_2CT_x MFs-based catalysts). The electrochemical durability is also an important indicator in evaluating the catalyst performance. As shown in Fig. 3f, the current

density remains a slightly decreasing upon potentiostatically cycling of the electrode at a large voltage of 1.9 V for 16 h, indicating an excellent recoverability due to the well-organized nanomeshes and microflower microstructures. The oxygen gas mass generated on the surface of catalysts could block some of the active sites (see Movie S1), leading to a decrease in current density in the constant potential test, compared with that of polarization curves [43]. Moreover, the microstructure of Mo_2CT_x MFs are completely maintained after a 16 h test (Figure S18), substantiating the excellent stability.

To compare the electrocatalytic activity of the Mo_2CT_x MFs and NMs with those of other non-noble metal-based OER catalysts reported to date, the η_{10} and the Tafel slopes are summarized in Fig. 3g (also see Table S2 for more details). By comparison, $\text{Ni}_x\text{Fe}_{1-x}\text{Se}_2$ -DO [44], FeCoW oxy-hydroxide [45], NiFe-MOF [46], CoFeNiO_x [47] and hierarchically structured, nitrogen-doped, graphitic nanoporous carbon membranes (HNDICMs) [2] achieve the lowest η_{10} and best kinetics compared with all the other reported systems. It can be seen that our Mo_2CT_x MFs and NMs achieve excellent performance for both catalytic activity and kinetics, and the Mo_2CT_x NM materials have become one of the best OER catalysts reported so far.

4. Discussion

Previous studies have implied that most transition metal compounds can be thermodynamically unstable and thus be easily oxidized into the corresponding metal oxides/hydroxides during OER [48]. Therefore, we have performed the electrochemical tests (Figure S19) and structural characterizations (Figure S20) to identify surface modification of

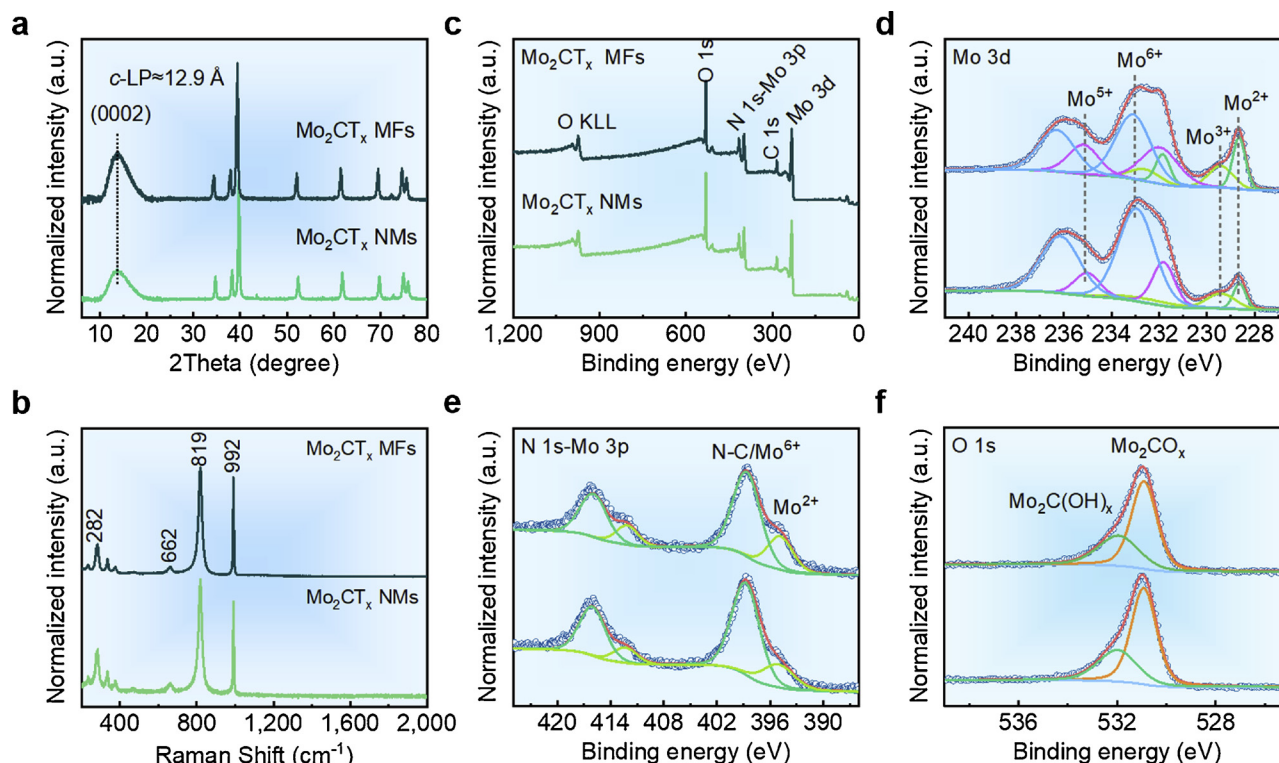


Fig. 2. Phase and surface terminations species analysis of Mo_2CT_x NMs and MFs. (a) XRD patterns. (b) Raman spectrum. (c) Full XPS spectrum. (d–f) Mo 3d (d), N 1s–Mo 3p (e) and O 1s (f) core level XPS spectra.

Mo_2CT_x NMs after OER. Our experimental results show that the surfaces of Mo_2CT_x NMs remain almost unchanged in the strong oxidative environment, where the formation of the corresponding Mo-based oxides/hydroxides is largely prevented, due to the unique structure and protection of surface oxygen terminations. Indeed, the stability in alkaline environment has been the major challenge for most of the non-oxide/hydroxide electrocatalysts, where they can steadily transform into metal hydroxides covering the surface quickly and then adversely affect the electrocatalytic performance. Considering the surface terminations of the catalytically active nanostructures (e.g. molybdenum carbides), there can be changes in the electronic properties of atoms close to surfaces [49]. X-ray absorption near edge structure (XANES) spectroscopy is a powerful technique that is widely used in studying the electronic and chemical structures of materials, and it has therefore been performed to characterize the active surface terminations of the Mo_2CT_x NMs and MFs catalysts. It is clear that the edge energy values of the Mo LIII-edge XANES spectra for the Mo_2CT_x NMs and MFs are located between those of pure Mo_2C and MoO_3 (Fig. 4a), indicating that oxygen species are formed on the surface of Mo_2C [50]. The white line in the XANES spectra that arises from an electronic transition between the 2p3/2 core level and the vacant 4d states is sensitive to the oxidation state of the Mo species [51]. The higher white line area for Mo_2CT_x NMs than that of the MFs suggests an increasing oxidation state, indicating that the hydrothermal reaction can result in intensification of the oxygen terminations, in good agreement with the XPS results (Table S1). To deeply clarify the difference, the 1st derivatives of XANES spectra are also presented in Fig. 4b. The energy changes significantly between pure Mo_2C (at 2520.6 eV) and the carbides have increased because of electron transfer from Mo to O. The analysis also suggests that this electron-rich oxygen terminations could become an active surface for electrochemical OER.

Why and how can the surface oxygen-rich terminations cause a sharp increase in the OER performance? We performed a series of partial density of states (PDOS) calculations (Fig. 4c) to clarify this question. The total density of states (DOS) shown in Figure S21

demonstrates that both oxygen-terminated and nitrogen terminated Mo_2C (Mo_2CO_x and Mo_2CN_x) show metallic character. Previous studies had demonstrated that the activation of H_2O molecules required electron transfer from the catalyst to H_2O [52]. The electron donation capacity of any catalyst can be determined based on the electronic population near the Fermi level [53]. Interestingly, the PDOS analysis suggests that the density of Mo 4d electrons near Fermi level decreases after oxidizing Mo_2C , reflecting the electron transferring from Mo to O, which is consistent with the XANES results. It is therefore worthy highlighting that the improved catalytic activity of Mo_2CT_x can well arise from the presence of electron-rich oxygen centers on the surface.

Another intriguing question is how the electron-rich oxygen species interact with reactants in Mo_2CO_x to yield the outstanding electrocatalytic OER activity (inset images of Fig. 4d). The OER process on Mo_2CO_x consisting of adsorption (step 1), dissociation (steps 2 and 3) and desorption (step 4) are summarized in Fig. 4d (see more calculated details in Tables S3–5). Obviously, the ΔG_1 of OH^+ on the N site (1.98 eV) exceeds that on the O site (0.99 eV), indicating easy formation of OH^+ on the O species. Two important facts can be concluded from a full survey of the Gibbs free energies. In comparison to Mo_2CN_x and Mo_2C , the lower ΔG_2 and ΔG_3 values of Mo_2CO_x indicate the easier dissociation of OH, favouring the intermediate reactions of the OER (Fig. 4d). In addition, the lower ΔG_4 value of Mo_2CO_x suggests easy desorption process of oxygen, agreeing well with the pattern of the electrochemical results (Fig. 3a).

The HER performance of Mo_2CT_x shows the reverse trend compared with the OER performance (Fig. 3c), suggesting that surface oxygen terminations are not conducive to their HER performance, as seen in a previous report [16]. The enhanced HER activity of Mo_2CT_x MFs over that of Mo_2CT_x NMs could well originate from the larger BET surface area ($52 \text{ m}^2 \text{ g}^{-1}$ for Mo_2CT_x MFs; $12 \text{ m}^2 \text{ g}^{-1}$ for Mo_2CT_x NMs, Figure S22a) and the broader mesopore distribution (Figure S22b). That could enable more active sites throughout the 3D scaffolds of the Mo_2CT_x MFs.

Mo sites with low valence states on the surfaces of Mo_2C have been

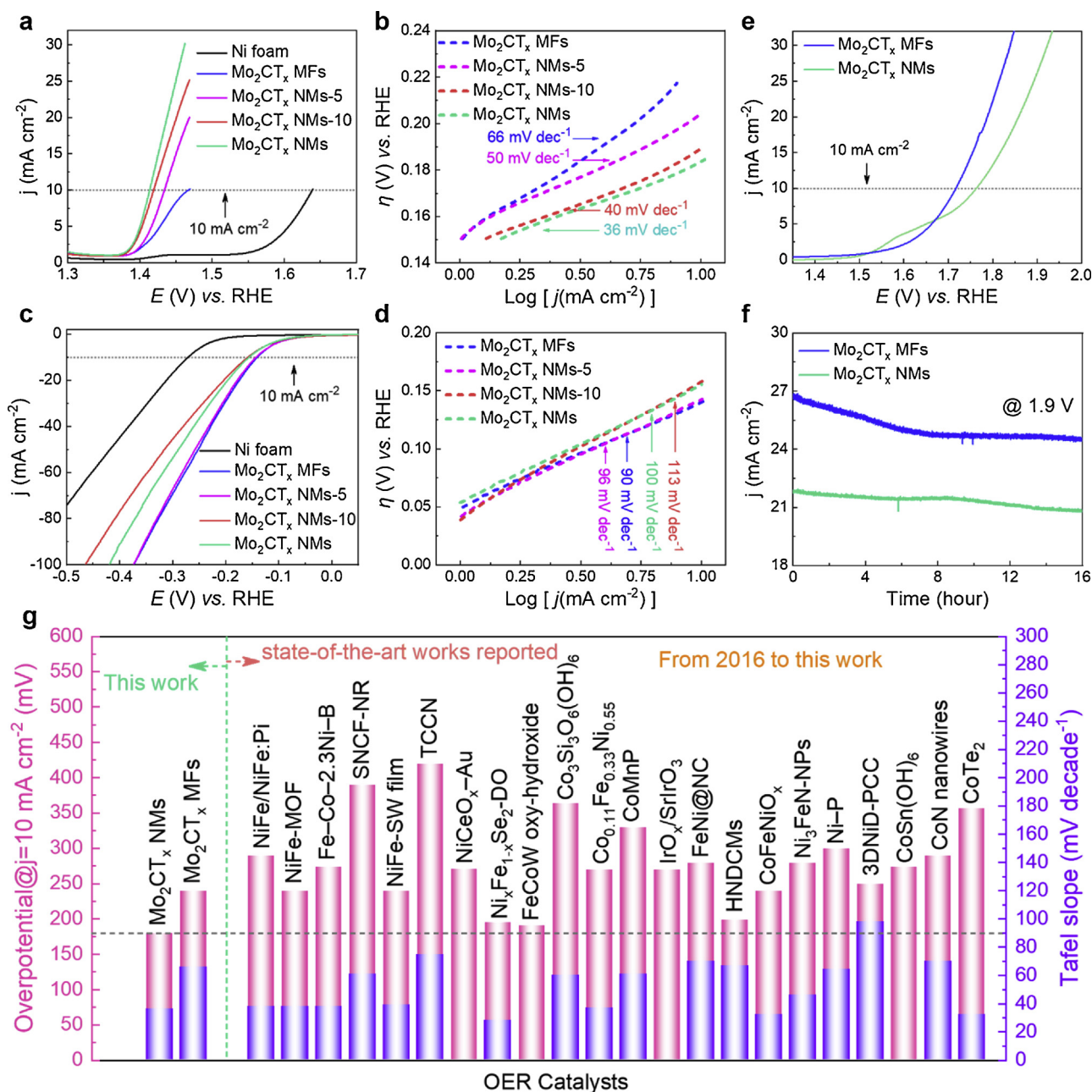


Fig. 3. Electrocatalytic OER, HER and overall water splitting performance in alkaline solution of Mo_2CT_x NMs and MFs. (a and b) LSV curves (a), and Tafel slopes (b) of various Mo_2CT_x NMs and MFs towards electrocatalytic OER in 1 M KOH. (c and d) LSV curves (c), and Tafel slopes (d) of various Mo_2CT_x NMs and MFs towards electrocatalytic HER. (e) LSV curves of Mo_2CT_x NMs and MFs as OER and HER bifunctional catalysts for overall water splitting (inset: digital photo of one 1.8 V battery driving Mo_2CT_x -based overall water splitting). (f) Time-dependent current density curves under the potential of 1.9 V. All catalysts are loaded into $1 \text{ cm}^2 \times 2 \text{ cm}$ Ni foam at a loading of 1 mg cm^{-2} . RHE, reversible hydrogen electrode. (g) OER activity comparison graph showing overpotentials at a current density of 10 mA cm^{-2} and Tafel slopes for state-of-the-art catalysts reported in the last three years. These data are collected from Table S2.

considered to be functional as the catalytic active sites towards HER [16]. Since abundant Mo sites are exposed across the porous 3D frameworks of Mo_2CT_x MFs, we have therefore considered that the different Mo sites on the surfaces can efficiently enhance the HER. For verification purposes, we undertook a series of DFT calculations. Figure S23a shows the geometries of the fully relaxed Mo_2C with three different hydrogen adsorption sites which are respectively named as H-Hollow, H-Bridge and H-Top sites. Compared pristine Mo_2C and Mo_2C with H-Hollow and H-Bridge sites, Mo_2C with the H-Top site shows an increasing PDOS for Mo 4d (0.99) and H 1s (0.14) near the Fermi level (Figure S23b), indicating an enhanced carrier density as well as d-band center (Figure S23c), along with highly efficient electron transfer from

surrounding atoms to the top Mo sites and to adsorbed H atoms (Figure S23d). In addition, ΔG_{H} has been widely adopted as an important indicator in the choice of appropriate HER catalysts [54]. A good catalyst should follow the Sabatier principle with $\Delta G_{\text{H}} \approx 0 \text{ eV}$, exactly as platinum [55]. As shown in Figure S23e, Mo_2C with a H-Top site presents the least negative ΔG_{H} of -0.19 eV compared with Mo_2C with the H-Hollow (-0.46 eV) and H-Bridge (-0.72 eV) sites. Consequently, top Mo sites on the surface could be responsible for the remarkable HER activity of Mo_2CT_x MFs. These results confirm that engineering surface oxygen terminations and constructing well-organized 3D frameworks of carbides containing electron-rich active sites can be a preferable pathway to design highly active catalysts.

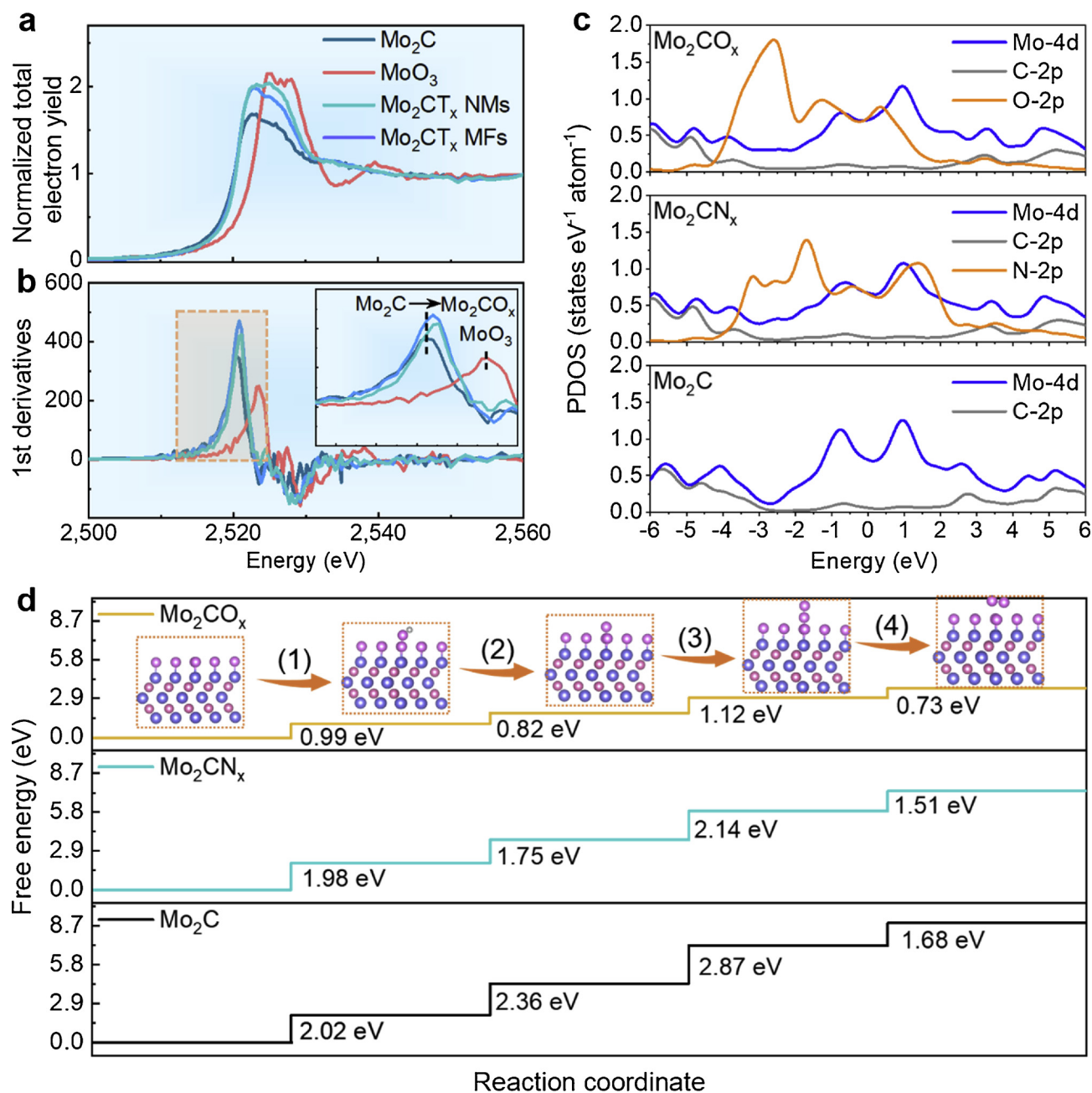


Fig. 4. XANES characterization and theoretical calculations towards OER. (a and b) Mo LIII-edge X-ray absorption near-edge structure (XANES) spectra (a), and 1st derivatives (b) collected on as-prepared Mo_2CT_x NMs and MFs, pure Mo_2C and MoO_3 as comparisons. (c) partial DOS calculations of Mo 4d, C 2p, N 2p and O 2p states of pure Mo_2C , oxygen terminated Mo_2C (Mo_2CO_x) and nitrogen terminated Mo_2C (Mo_2CN_x). (d) Standard free energy diagram of the OER process on Mo_2CO_x and Mo_2CN_x surfaces. Inset shows image of the primitive steps of the OER process. Colour scheme for chemical representation: red for carbon, pink for oxygen, gray for hydrogen and cyan for molybdenum (For interpretation of the references to colour in this figure legend, the reader is referred to the web version of this article.).

5. Conclusion

In summary, 2D molybdenum carbide nanomeshes and their assembled 3D microflowlers (Mo_2CT_x NMs and MFs, respectively) have been successfully prepared by rationally designing novel Mo/Zn bi-metal imidazole frameworks (Mo/Zn BIFs) and pyrolyzing them. When used as bifunctional electrocatalysts for OER and HER, they exhibit outstanding electrocatalytic performance. Significantly, atomic level surface engineering endows the Mo_2CT_x NMs with the highest OER activity reported so far. Further, they demonstrate the desired stability in alkaline environment, which has been a major challenge for most of the non-oxides/hydroxides electrocatalysts due to the formation of metal hydroxides on surface. The formation of Mo-based oxides/

hydroxides is largely prevented, due to the unique structure and protection of surface oxygen terminations. The chiseled surface atomic structure of Mo_2CT_x NMs enables us to probe the nature behind excellent OER activity where the oxygen terminations provide the main active centers towards OER. Its HER activity can be optimized by increasing top Mo active sites on the surface. We conclude that the surface chemistry modification and multiscale structure design demonstrated in the present work are effective strategies towards atomic level engineering of active catalysts.

Acknowledgement

We thank support of Ministry of Education (MOE), Singapore

(MOE2016-T2-2-138) for funding of research, conducted at the National University of Singapore.

Appendix A. Supplementary data

Supplementary material related to this article can be found, in the online version, at doi:<https://doi.org/10.1016/j.apcatb.2018.11.008>.

References

- [1] I. Roger, M.A. Shipman, M.D. Symes, *Nat. Rev. Chem.* 1 (2017) 0003.
- [2] H. Wang, S. Min, C. Ma, Z. Liu, W. Zhang, Q. Wang, D. Li, Y. Li, S. Turner, Y. Han, *Nat. Commun.* 8 (2017) 13592.
- [3] H. Li, S. Chen, X. Jia, B. Xu, H. Lin, H. Yang, L. Song, X. Wang, *Nat. Commun.* 8 (2017) 15377.
- [4] Y. Xu, W. Tu, B. Zhang, S. Yin, Y. Huang, M. Kraft, R. Xu, *Adv. Mater.* 29 (2017) 1605957.
- [5] C. Tang, R. Zhang, W. Lu, L. He, X. Jiang, A.M. Asiri, X. Sun, *Adv. Mater.* 29 (2017) 1602441.
- [6] C. Tang, R. Zhang, W. Lu, Z. Wang, D. Liu, S. Hao, G. Du, A.M. Asiri, X. Sun, *Angew. Chem. Int. Ed* 56 (2017) 842.
- [7] H. Lv, Z. Xi, Z. Chen, S. Guo, Y. Yu, W. Zhu, Q. Li, X. Zhang, M. Pan, G. Lu, *J. Am. Chem. Soc.* 137 (2015) 5859.
- [8] B. Han, K.A. Stoerzinger, V. Tileli, A.D. Gamalski, E.A. Stach, Y. Shao-Horn, *Nat. Mater.* 16 (2017) 121.
- [9] A. Grimaud, O. Diaz-Morales, B. Han, W.T. Hong, Y.-L. Lee, L. Giordano, K.A. Stoerzinger, M.T. Koper, Y. Shao-Horn, *Nat. Chem.* 9 (2017) 457.
- [10] T. Ling, D.-Y. Yan, H. Wang, Y. Jiao, Z. Hu, Y. Zheng, L. Zheng, J. Mao, H. Liu, X.-W. Du, *Nat. Commun.* 8 (2017) 1509.
- [11] Y. Jia, L. Zhang, G. Gao, H. Chen, B. Wang, J. Zhou, M.T. Soo, M. Hong, X. Yan, G. Qian, *Adv. Mater.* 29 (2017) 1700017.
- [12] D. Escalera-López, Y. Niu, S.J. Park, M. Isaacs, K. Wilson, R.E. Palmer, N.V. Rees, *Appl. Catal., B* 235 (2018) 84.
- [13] Z. Pu, I.S. Amiinu, Z. Kou, W. Li, S. Mu, *Angew. Chem. Int. Ed.* 56 (2017) 11559.
- [14] J. Wang, F. Xu, H. Jin, Y. Chen, Y. Wang, *Adv. Mater.* 29 (2017) 1605838.
- [15] Z. Kou, K. Xi, Z. Pu, S. Mu, *Nano Energy* 26 (2017) 374.
- [16] Z. Kou, T. Wang, Y. Cai, C. Guan, Z. Pu, C. Zhu, Y. Hu, A.M. Elshahawy, J. Wang, S. Mu, *Small Methods* 2 (2018) 1700396.
- [17] M. Yan, X. Pan, P. Wang, F. Chen, L. He, G. Jiang, J. Wang, J.Z. Liu, X. Xu, X. Liao, *Nano Lett.* 17 (2017) 4109.
- [18] S. Gupta, N. Patel, R. Fernandes, R. Kadrekar, A. Dashora, A.K. Yadav, D. Bhattacharyya, S.N. Jha, A. Miotello, D.C. Kothari, *Appl. Catal., B* 192 (2016) 126.
- [19] Y. Zhong, X. Xia, F. Shi, J. Zhan, J. Tu, H.J. Fan, *Adv. Sci.* 3 (2016) 1500286.
- [20] J.-S. Li, Y. Wang, C.-H. Liu, S.-L. Li, Y.-G. Wang, L.-Z. Dong, Z.-H. Dai, Y.-F. Li, Y.-Q. Lan, *Nat. Commun.* 7 (2016) 11204.
- [21] S. Jing, L. Zhang, L. Luo, J. Lu, S. Yin, P.K. Shen, P. Tsiakaras, *Appl. Catal., B* 224 (2018) 533.
- [22] W.S. Zhi, K.D. Fredrickson, B. Anasori, J. Kibsgaard, A.L. Strickler, M.R. Lukatskaya, Y. Gogotsi, T.F. Jaramillo, A. Vojvodic, *ACS Energy Lett.* 1 (2016) 589.
- [23] T.Y. Ma, J.L. Cao, M. Jaroniec, S.Z. Qiao, *Angew. Chem. Int. Ed.* 55 (2016) 1138.
- [24] B. Anasori, M.R. Lukatskaya, Y. Gogotsi, *Nat. Rev. Chem.* 2 (2017) 16098.
- [25] Y. Yang, H. Fei, G. Ruan, C. Xiang, J.M. Tour, *Adv. Mater.* 26 (2014) 8163.
- [26] H. Zou, B. He, P. Kuang, J. Yu, K. Fan, *Adv. Funct. Mater.* 28 (2018) 1706917.
- [27] Y.C. Chen, A.Y. Lu, P. Lu, X. Yang, C.M. Jiang, M. Mariano, B. Kaehr, O. Lin, A. Taylor, I.D. Sharp, *Adv. Mater.* 29 (2017) 1703863.
- [28] J. Deng, H. Li, S. Wang, D. Ding, M. Chen, C. Liu, Z. Tian, K.S. Novoselov, C. Ma, D. Deng, X. Bao, *Nat. Commun.* 8 (2017) 14430.
- [29] Y.P. Zhu, C. Guo, Y. Zheng, S.-Z. Qiao, *Acc. Chem. Res.* 50 (2017) 915.
- [30] P. Martián-Zarza, J.M. Arrieta, M.C. Muñoz-Roca, P. Gili, *J. Chem. Soc., Dalton Trans.* 0 (1993) 1551.
- [31] T. Wang, Z. Kou, S. Mu, J. Liu, D. He, I.S. Amiinu, W. Meng, K. Zhou, Z. Luo, S. Chaemchuen, *Adv. Funct. Mater.* 28 (2017) 1705048.
- [32] P. Basu, A.M. Raitsimring, M.J. LaBarre, I.K. Dhawan, J.L. Weibrecht, J.H. Enemark, *J. Am. Chem. Soc.* 116 (1994) 7166.
- [33] Y. Zheng, Y. Jiao, S.Z. Qiao, *Adv. Mater.* 27 (2015) 5372.
- [34] J. Jia, T. Xiong, L. Zhao, F. Wang, H. Liu, R. Hu, J. Zhou, W. Zhou, S. Chen, *ACS Nano* 11 (2017) 12509.
- [35] H. Kim, B. Anasori, Y. Gogotsi, H.N. Alshareef, *Chem. Mater.* 29 (2017) 6472.
- [36] P.F. Liu, S. Yang, L.R. Zheng, B. Zhang, H.G. Yang, *Chem. Sci.* 8 (2017) 3484.
- [37] Z. Kou, T. Meng, B. Guo, I.S. Amiinu, W. Li, J. Zhang, S. Mu, *Adv. Funct. Mater.* 27 (2017) 1604904.
- [38] J. Halim, S. Kota, M.R. Lukatskaya, M. Naguib, M.Q. Zhao, E.J. Moon, J. Pitock, J. Nanda, S.J. May, Y. Gogotsi, *Adv. Funct. Mater.* 36 (2016) 3118.
- [39] Y. Zhu, G. Chen, X. Xu, G. Yang, M. Liu, Z. Shao, *ACS Catal.* 7 (2017) 3540.
- [40] P. Xiao, X. Ge, H. Wang, Z. Liu, A. Fisher, X. Wang, *Adv. Funct. Mater.* 25 (2015) 1520.
- [41] Q. Gong, Y. Wang, Q. Hu, J. Zhou, R. Feng, P.N. Duchesne, P. Zhang, F. Chen, N. Han, Y. Li, *Nat. Commun.* 7 (2016) 13216.
- [42] M.J. Kim, S. Kim, D.H. Song, S.K. Oh, K.J. Chang, E.A. Cho, *Appl. Catal., B* 227 (2018) 340.
- [43] J. Chang, Q. Lv, G. Li, J. Ge, C. Liu, W. Xing, *Appl. Catal., B* 204 (2017) 486.
- [44] X. Xu, F. Song, X. Hu, *Nat. Commun.* 7 (2016) 12324.
- [45] B. Zhang, X. Zheng, O. Voznyy, R. Comin, M. Bajdich, M. García-Melchor, L. Han, J. Xu, M. Liu, L. Zheng, *Science* 352 (2016) 333.
- [46] J. Duan, S. Chen, C. Zhao, *Nat. Commun.* 8 (2017) 15341.
- [47] C.G. Morales-Guio, L. Liardet, X. Hu, *J. Am. Chem. Soc.* 138 (2016) 8946.
- [48] J. Song, *ACS Energy Lett.* 2 (2017) 1937.
- [49] Y. Xie, M. Naguib, V.N. Mochalin, M.W. Barsoum, Y. Gogotsi, X. Yu, K.-W. Nam, X.-Q. Yang, A.I. Kolesnikov, P.R. Kent, *J. Am. Chem. Soc.* 136 (2014) 6385.
- [50] H. Aritani, S. Shinohara, S.-i. Koyama, K. Otsuki, T. Kubo, A. Nakahira, *Chem. Lett.* 35 (2006) 416.
- [51] J.S. Lee, J.E. Yie, *Korean J. Chem. Eng.* 8 (1991) 164.
- [52] C. Ling, L. Shi, Y. Ouyang, X.C. Zeng, J. Wang, *Nano Lett.* 17 (2017) 5133.
- [53] S. Zhao, Y. Wang, J. Dong, C.-T. He, H. Yin, P. An, K. Zhao, X. Zhang, C. Gao, L. Zhang, *Nat. Energy* 1 (2016) 16184.
- [54] Z. Kou, T. Wang, Z. Pu, L. Wu, K. Xi, S. Mu, *Nanoscale Horiz.* (2018), <https://doi.org/10.1039/C8NH00275D>.
- [55] J. Greeley, T.F. Jaramillo, J. Bonde, I. Chorkendorff, J.K. Nørskov, *Nat. Mater.* 5 (2006) 909.